catalysts

Article

Evidence of Synergy Effects between Zinc and Copper Oxides with Acidic Sites on Natural Zeolite during Photocatalytic Oxidation of Ethylene Using Operando DRIFTS Studies

Norberto J. Abreu [1,2,3,*], Héctor Valdés [1,*], Claudio A. Zaror [4], Tatianne Ferreira de Oliveira [5], Federico Azzolina-Jury [6] and Frédéric Thibault-Starzyk [6]

[1] Laboratorio de Tecnologías Limpias, Facultad de Ingeniería, Universidad Católica de la Santísima Concepción, Alonso de Ribera 2850, Concepción 4030000, Chile
[2] Departamento de Ingeniería Química, Facultad de Ingeniería y Ciencias, Universidad de la Frontera, Francisco Salazar 01145, Temuco 4780000, Chile
[3] Center of Waste Management and Bioenergy, Scientific and Technological Bioresources Nucleus, Universidad de la Frontera, Francisco Salazar 01145, Temuco 4780000, Chile
[4] Departamento de Ingeniería Química, Facultad de Ingeniería, Universidad de Concepción, Edmundo Larenas s/n, Concepción 4030000, Chile
[5] School of Agronomy, Federal University of Goiás, Goiânia 74690-900, Brazil
[6] Laboratoire Catalyse et Spectrochimie, Normandie Univ, ENSICAEN, UNICAEN, CNRS, 14050 Caen, France
* Correspondence: norberto.abreu@ufrontera.cl (N.J.A.); hvaldes@ucsc.cl (H.V.)

Abstract: In this article, the role of surface sites of modified zeolites with semiconductor nanoparticles as alternative photocatalyts for protecting post-harvest foodstuff from the detrimental effects of ethylene is addressed. Two single and one double catalyst based on zinc and copper oxides supported over modified zeolite samples were prepared. Physical, chemical, and surface properties of prepared materials were studied by several characterization methods. UV-Vis absorption spectra show that the applied modification procedures increase the optical absorption of light in the UV and visible regions, suggesting that an increase in the photocatalytic activity could take place mainly in the obtained co-impregnated catalyst. An ethylene conversion around 50% was achieved when the parent natural zeolite support was modified with both transition metal oxides, obtaining higher removal efficiency in comparison to single oxide catalysts. Adsorption and photocatalytic oxidation experiments were also performed using single and double catalysts supported over fumed silica, attaining lower ethylene conversion and thus highlighting the role of zeolite surfaces as adsorption sites for ethylene during photocatalytic reactions. *Operando* diffuse reflectance infrared Fourier transform spectroscopy (DRIFTS) studies reveal that a synergistic mechanism occurs, involving ethylene adsorption at acidic sites of zeolite and its photocatalytic oxidation due to the generation of radicals by the light activation of nanoparticles of zinc and copper oxides.

Keywords: adsorption; natural zeolite support; single and double metal oxide catalysts; photocatalysis; synergistic mechanism

check for updates

Citation: Abreu, N.J.; Valdés, H.; Zaror, C.A.; de Oliveira, T.F.; Azzolina-Jury, F.; Thibault-Starzyk, F. Evidence of Synergy Effects between Zinc and Copper Oxides with Acidic Sites on Natural Zeolite during Photocatalytic Oxidation of Ethylene Using Operando DRIFTS Studies. *Catalysts* **2023**, *13*, 610. https://doi.org/10.3390/catal13030610

Academic Editors: De Fang and Yun Zheng

Received: 11 February 2023
Revised: 12 March 2023
Accepted: 14 March 2023
Published: 17 March 2023

1. Introduction

Ethylene is regarded as a gaseous multifunctional phytohormone that regulates growth and senescence of plants and fruits [1]. Even at a low concentration and temperature, ethylene can accelerate the ageing and spoiling of harvested fruits [2]. This powerful plant hormone cause effects at part-per-million (ppm) to part-per-billion (ppb) concentrations, affecting both the aesthetics and function of climacteric and non-climacteric fruit and vegetables [1]. For example, in the case of climacteric fruit such as bananas, tomatoes, apricots, and apples, the exposition to ethylene concentrations from 0.01 to 0.5 $\mu L\ L^{-1}$ could induce shrinkage and decay. Moreover, high score registration of loss in fruit sensitive to ethylene was reported in the United Kingdom, where at least 1.4 million bananas and 1.5 million tomatoes were wasted daily in 2010, mainly caused by ethylene mediated effects [3]. Moreover, studies conducted in Germany during the same year mentioned that around 50% of food waste belongs to fruit and vegetables directly related with ripening induced by ethylene [4]. Hence, the control and removal of ethylene from fruits' environment is an important challenge for improving their quality and increasing their shelf life [5,6]. For such purpose, several methods have been focused on the removal of ethylene, including ventilation, recuperative adsorption, and techniques concerning destructive oxidation [7]. Among these methods, the combination of adsorbents with photocatalytic materials for the oxidation of ethylene was suggested as a very promising and cost-effective technique [7].

As a result of their specific properties, different structures of zeolites have been used for ethylene adsorption such as mordenite [8], clinoptilolite [9,10], and some synthetic zeolites [11–13]. Zeolites can be used as adsorbent materials or as supports in photocatalytic applications. Mechanical, physical, and chemical characteristics such as high mechanical resistance, individual microporous and mesoporous structure, the presence of Brønsted and Lewis acid sites, and a great ion-exchange capacity allow zeolites to be used in different applications [14,15]. It has been indicated that the exchange of compensating cations originally presented at zeolite surface by specific cations, increases the selectivity of the adsorption towards several compounds, including ethylene [16–19].

In the last years, the combined effect of photocatalysis and adsorption in the removal of pollutants has been of significant interest for the scientific community [14,20]. It has been claimed that such combination allows the concentration of the contaminants near photocatalytic active sites, promoting photocatalytic reactions, increasing the adsorption of the intermediaries, and the re-use of the adsorbent [15]. Although studies concerning both combined processes have been conducted [15,20], there is still a lack of experimental evidence about the role of the active sites in the reaction mechanism. Results presented here address this issue.

Semiconductor materials with a wide band gap, such as titanium dioxide (e.g., ~3.2 eV for anatase phase), has been extensively used as an effective photocatalyst due to its capacity to totally oxidize organic pollutants, its chemical stability, among some other properties [21,22]. However, it has been reported that TiO_2 tends to lose its activity during the photocatalytic oxidation of contaminants because of a decrease in the number of active sites on the catalyst surface, leading to the search of alternative materials [23,24]. Besides TiO_2, there are several materials that present excellent photocatalytic activities under UV light with a wide band gap energy. For instance, graphitic carbon nitride (g-C_3N_4), a photocatalyst with high stability and adequate light adsorption [25]; bismuth oxychloride (BiOCl), a novel semiconductor material used recently in the degradation of caffeic and gallic acids [26]; zinc oxide, an environmentally friendly catalyst used in the degradation and mineralization of environmental pollutants [27]; and some other semiconductor materials.

Among them, zinc oxide has emerged as a non-toxic, very common in nature n-type oxide semiconductor with a wide band gap (3.37 eV) and absorption bands in the UV spectra that can be used in several applications such as for cytotoxicity, antibacterial activities, solar cells, electrical and optical devices as well as in photocatalytic applications [28]. It has a high thermal and electro-chemical stability. It is also relatively cheap due to its high availability in nature [29]. Zinc oxide stands out for its high photocatalytic efficiency in the mineralization of organic contaminants in comparison to other similar semiconductors, including even TiO_2, as well as for its high stability [21]. The photocatalytic activity of ZnO has been proved several times, showing excellent results in the degradation of organic compounds such as rose bengal [30], methyl orange [31], rhodamine B [32], and some other emergent contaminants [33].

Recently, it has been suggested that the photocatalytic activity of zinc oxide can be enhanced and extended to the visible spectrum by doping with metal ions or by creating structures on the surface with lower energy gap semiconductors [34]. Copper oxide is a *p*-type semiconductor oxide with a narrow band gap (1.2 eV) [35] and can be excited even with radiation of visible spectrum [20]. Excellent photocatalytic results have come due to the modification of zinc oxide with copper oxide nanoparticles [36,37]. The high availability, excellent physico-chemical properties, and the low cost of copper make it an attractive material for applied research and encourage its recent use as a catalyst in several applications. Photocatalytic materials containing CuO have also been applied in the oxidation of organic pollutants such as methylene blue [38,39] and methyl orange [40] among several organic contaminants [41].

Double catalysts, such as zinc and copper oxides supported on modified natural zeolite, could enhance the photocatalytic activity by increasing the electron–hole pair separation efficiency and also by diminishing the recombination of generated electron–hole pairs by the mutual transfer of electrons or holes between both semiconductors [37], whereas acidic surface sites of zeolite could contribute to the retention of the adsorbed molecules near photocatalytic sites, enhancing catalytic performance.

Most of the research efforts for ethylene elimination have considered adsorption and photocatalysis as separated processes [7–11,42,43]. Although some authors used zinc oxide and copper oxide as single or bimetallic oxide heterojunctions supported on zeolites for photocatalysis [44–46], these works were mainly focused on removal rate and reaction kinetics. In this work, *operando* diffuse reflectance infrared Fourier transform spectroscopy (DRIFTS) studies were applied to unveil the chemical interactions that take place between ethylene molecules and active surface sites of modified zeolite with supported single and double zinc and copper oxides during the photocatalytic oxidation of ethylene. This work was focused on studying the synergistic ethylene adsorption/photocatalytic oxidation mechanism by considering the evolution of the infrared bands of the active sites under *operando* DRIFTS assays. Moreover, to assess the effect of the support in the reaction mechanism, fumed silica was used in control experiments as a support of metal oxides. Additionally, TiO_2 was mixed with the raw fumed silica and used as a benchmark photocatalyst for comparison. As a result, a surface reaction mechanism is proposed.

2. Results and Discussion

2.1. Physico-Chemical Characteristics

Chemical analyses of all samples are presented in Table 1. ***Nitrogen adsorption isotherms*** at 77 K reveal a combination of characteristic type I and IV isotherms, related to microporous and mesoporous structure behavior of the zeolite samples, respectively (see Figure S1 in Supplementary Materials) [47]. Due to the removal of impurities in the parent zeolite, the surface area increases and the Si/Al ratio diminishes by around 9% after the double ion exchange conducted using the $(NH_4)_2SO_4$ solution followed by a thermal outgassing at 623 K (see Table 1). However, subsequent modifications with transition metals diminish the surface areas, mainly in the samples impregnated with zinc oxides.

Table 1. Physical–chemical surface properties of parent zeolite and fumed silica supports and single and double metal oxide catalysts supported on modified natural zeolite and on fumed silica.

Samples	S_{BET} [a] $[m^2\ g^{-1}]$	V_{micro} [a] $[cm^3\ g^{-1}]$	V_{meso} [a] $[cm^3\ g^{-1}]$	Si/Al [b]	Si [b,c] [%]	Al [b,c] [%]	Ca [b,c] [%]	Na [b,c] [%]	Fe [b,c] [%]	Ti [b,c] [%]	Mg [b,c] [%]	Zn [b,c] [%]	Cu [b,c] [%]
Z_Nat	280.88	0.07	0.14	5.32	65.39	12.29	11.13	2.12	5.27	0.89	0.53	0.02	ND
ZH	358.24	0.12	0.10	5.44	71.13	13.07	6.83	0.38	5.66	0.90	0.30	0.02	ND
ZH_Cu	281.58	0.07	0.12	4.94	65.99	13.36	3.65	0.30	2.25	0.44	0.39	0.02	12.16
ZH_Zn	203.17	0.06	0.12	5.02	68.67	13.67	3.07	0.32	2.12	0.43	0.32	10.95	ND
ZH_Zn/Cu	261.40	0.04	0.13	5.01	68.42	13.65	3.03	0.41	2.16	0.44	0.31	5.42	5.42
FS	261.02	ND	0.32	ND	100.0	ND	ND	ND	ND	ND	ND	ND	ND
FS_Cu	242.35	ND	0.31	ND	92.20	ND	ND	ND	ND	ND	ND	ND	7.80
FS_Zn	224.80	ND	0.31	ND	92.11	ND	ND	ND	ND	ND	ND	7.89	ND
FS_Zn/Cu	220.29	ND	0.26	ND	92.07	ND	ND	ND	ND	ND	ND	3.78	4.15

[a] Determined by nitrogen adsorption/desorption at 77 K. [b] Zeolite supported samples composition determined by X-ray fluorescence. [c] Fumed silica supported samples composition determined by energy dispersive X-ray spectroscopy.

Results obtained from ***XRD diffractograms*** shown in Figure 1 reveal that the mineralogical and structural composition of the parent zeolite is not significantly changed after all the applied chemical and thermal treatments. The higher intensity peaks correspond to clinoptilolite (JCPDS 39-183), mordenite (JCPDS 29-1257), and quartz (JCPDS 46-1045). Such peaks remain with similar intensity after the applied modification procedures. Moreover, the peaks related to copper oxide (JCPDS 48-1548) and zinc oxide (JCPDS 36-1451) can be identified in the diffractograms of the modified samples.

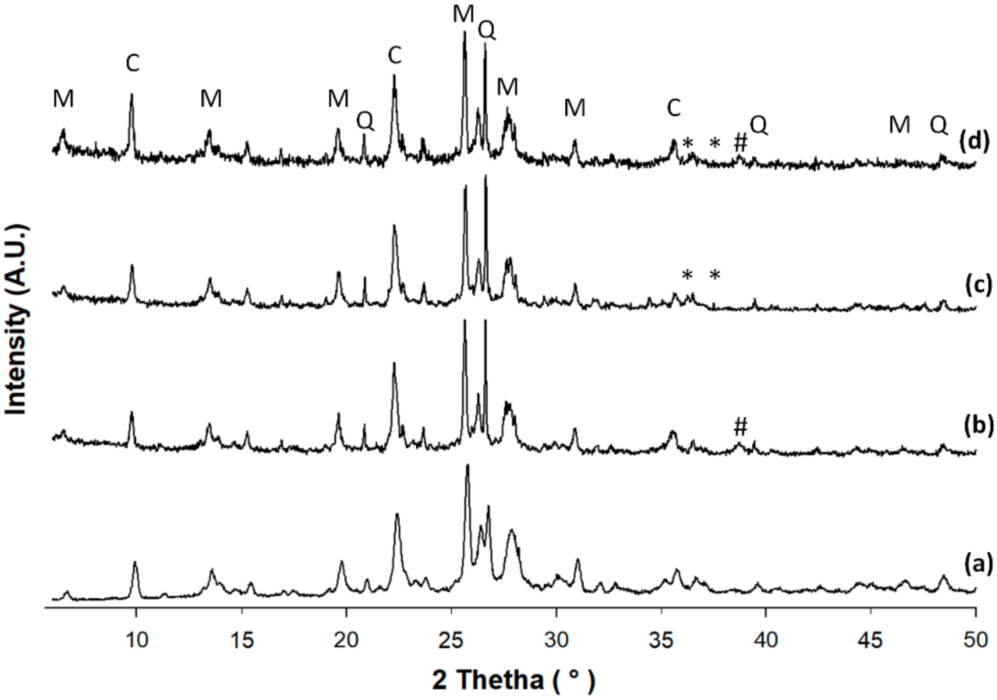

Figure 1. X-ray diffraction patterns of parent zeolite support and prepared single and double metal oxide catalysts supported on modified natural zeolite. (**a**) ZNAT; (**b**) ZH_Cu; (**c**) ZH_Zn; (**d**) ZH_Zn/Cu. M: Mordenite, C: Clinoptilolite, Q: Quartz, #: copper oxide, *: zinc oxide.

Morphological structures, as observed by ***Scanning Electron Microscopy images,*** are depicted for zeolite samples in Figure 2A,C–E. SEM images reveal porous lamellar morphologies with individual zeolite crystals around a 40–70 nm width. Similar results were reported in clinoptilolite pore network studies by other authors [48]. Meanwhile, for fumed silica samples (see Figure 2B,F–H), individual quasi-spherical shaped particles around 60 µm were observed with an evident porous structure. The porous characteristics were confirmed by nitrogen adsorption/desorption assays (see Table 1 and Figures S1 and S2 in Supplementary Materials); however, in those samples supported on fumed silica, only a mesoporosity network was found without a microporous structure. In the case of zeolite samples, the surface area reduction after conducting the modification with transition metals can be associated to the formation of metal oxide nanoparticles and their agglomeration, generating particles of a bigger size inside the zeolite porous structure that can block nitrogen diffusion. SEM and transmission electron microscopy (TEM) images corroborate such findings (Figures 2 and 3).

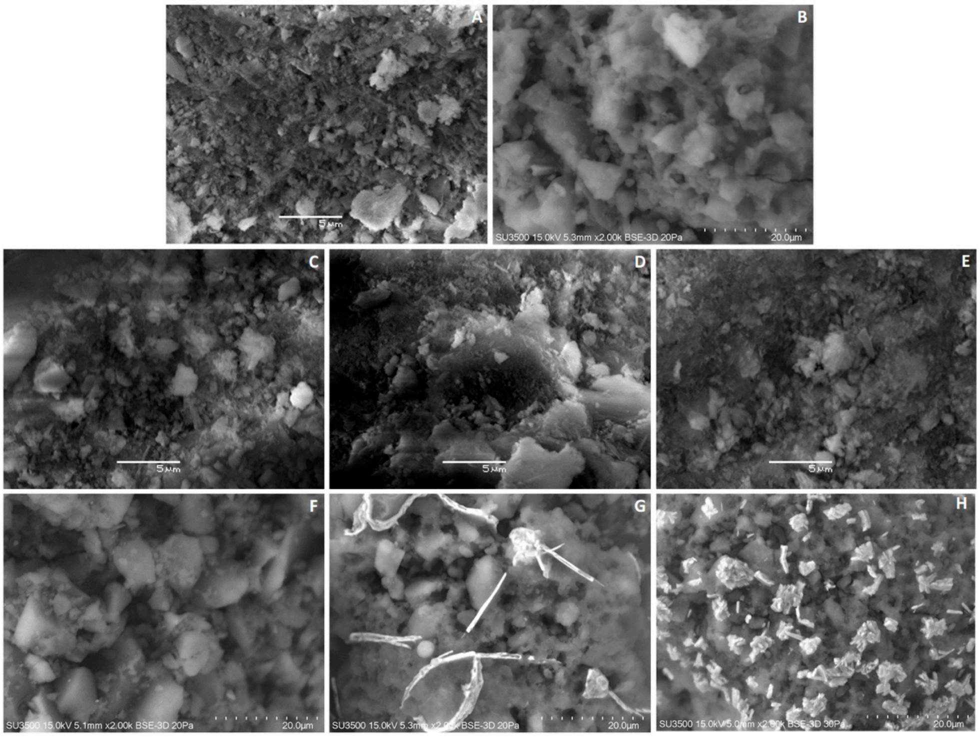

Figure 2. Scanning electron microscopy images of parent zeolite support and prepared single and double metal oxide catalysts supported on modified natural zeolite: (**A**) ZNAT; (**B**) FS; (**C**) ZH_Cu; (**D**) ZH_Zn; (**E**) ZH_Zn/Cu; (**F**) FS_Cu; (**G**) FS_Zn; (**H**) FS_Zn/Cu.

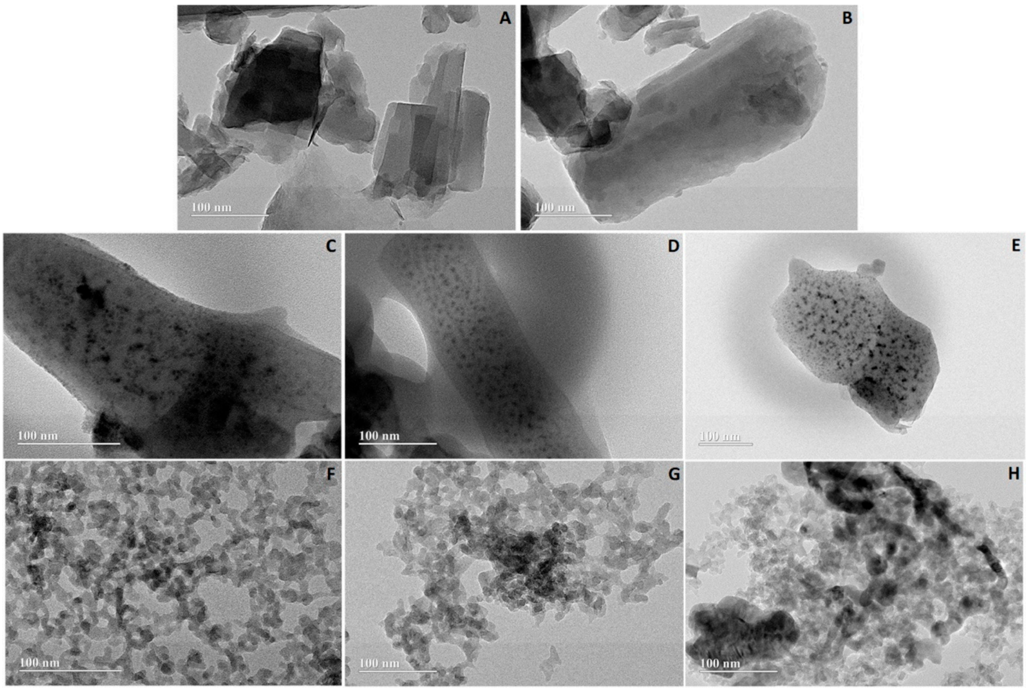

Figure 3. Transmission electron microscopy images of parent zeolite support and prepared single and double metal oxides supported on modified natural zeolite and fumed silica: (**A**) ZNAT; (**B**) ZH; (**C**) ZH_Cu; (**D**) ZH_Zn; (**E**) ZH_Zn/Cu; (**F**) FS_Cu; (**G**) FS_Zn; and (**H**) FS_Zn/Cu.

Additionally, ***Transmission Electron Microscopy images*** displayed in Figure 3 corroborate the lamellar morphology and depict the incorporation of metal oxide nanoparticles on the zeolite surface. Results show that the sequence of ion exchange and wet impregnation procedures using transition metal salts followed by the calcination treatment at 623 K do not only exchange compensating cations presented in the zeolite sample, but also generate nanoparticles of metal oxides (see Figure 3C–E). The formation of small oxide particles around 10.01 ± 2.5 nm of diameters are obtained when only copper salt is used (Figure 3C). However, when zinc nitrate is applied as a precursor for zinc oxide formation, metal oxide nanoparticles of slightly higher sizes can be observed with particle sizes of 12.2 ± 3.20 nm and 13.9 ± 3.65 nm (Figure 3D,E) for ZH_Zn and ZH_Zn/Cu, respectively. Such results suggest that during zinc oxide formation, particles flocculate, leading to the clustering of small particles and the formation of bigger metal oxide particles. During the impregnation step, water is evaporated and concentrated transition metal salts are deposited onto zeolite surface that later are decomposed during the calcination procedure, driving the generation of the observed metal oxide nanoparticles. The generation of aggregates of nanoparticles of a bigger size can explain the reduction in the surface area values listed in Table 1 for such samples. Moreover, in the oxide supported catalysts over fumed silica (see Figure 3F–H), a similar behavior was observed. However, in those cases, slightly higher particle sizes were observed in the TEM assay. Particles of 11.5 ± 4.1 nm, 13.2 ± 3.9 nm nm, and 14.7 ± 3.7 nm can be seen at FS_Cu, FS_Zn, and FS_Zn/Cu samples, respectively. Such findings could be related to the existence of larger pores in the fumed silica as compared to natural zeolite as it was observed during porosimetry measurements (see Table 1).

The ***UV-visible*** absorbance spectra of parent zeolite and fumed silica supports and prepared single and double metal oxide catalysts supported on modified natural zeolite and fumed silica are displayed in Figure 4A,B, respectively. Light absorption spectra acquired by ultraviolet-visible diffuse reflectance spectroscopy (UV-Vis DRS) were transformed to Tauc plots to determine the optical band gap energy of each assessed material (Figure 4C,D) [49]. The band gap energy was calculated by extrapolating the linear part of the vertical region of the curve [50,51].

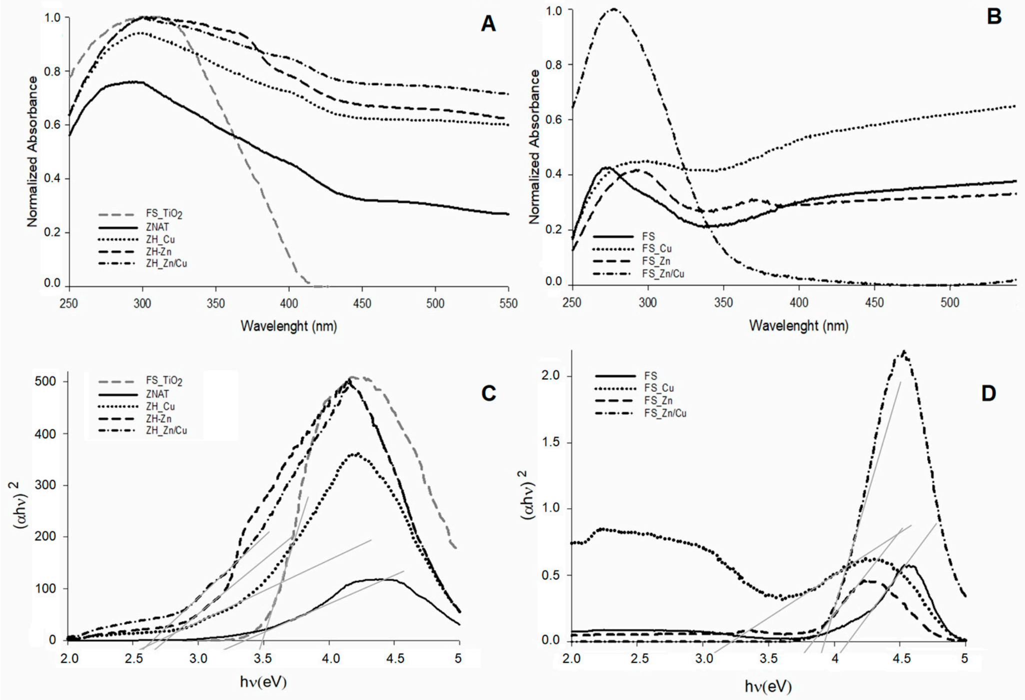

Figure 4. UV-visible absorbance spectra (upper part) and Tauc plots (bottom part) of parent supports and prepared single and double metal oxide catalysts supported on modified natural zeolite (**A**,**C**), and fumed silica (**B**,**D**). Additionally, TiO_2 (**A**,**C**) is included as a benchmarked photo-catalyst.

As it can be seen in Figure 4A, the incorporation of copper and zinc oxides onto the surface of natural zeolite increases the optical absorption in the UV and visible regions.

Thus, the values of the band gap energy in the zeolite samples decrease in the following order: ZH_Zn/Cu < ZH_Cu < ZH_Zn < ZNat (see Figure 4C and Table 2). Moreover, a similar behavior regarding optical absorption was observed in the catalysts supported on fumed silica; however, the band gap energies are higher than those obtained from the catalysts supported on modified zeolite. In such cases, the band gap energies present the following trend: FS_Cu < FS_Zn < FS_Zn/Cu < FS (see Figure 4D and Table 2).

Table 2. Band gap energies of prepared photo-catalysts, including their respective supports. Results were obtained by UV-Vis DRS spectroscopy.

Samples	**Band Gap Values (eV)**
Z_Nat	3.35
ZH_Cu	2.70
ZH_Zn	2.75
ZH_Zn/Cu	2.65
FS	4.20
FS_Cu	3.20
FS_Zn	3.85
FS_Zn/Cu	3.90
FS_TiO_2	3.50

It is important to notice that zeolite supported samples present higher light absorbance than fumed silica samples. Fumed silica is a transparent material which transmit most of incident light, whereas zeolite is an opaquer material, increasing the light absorption in the support. Hence, copper-based materials used here present different trends regarding band gap measurements when they are deposited over the different supports. Indeed, double catalyst samples also show differences. When zeolite is used as a support material (ZH_Zn/Cu), a better particle dispersion was obtained, suggesting the formation of an heterostrucure where exited electrons from the higher band gap material are trapped by the surface of the deposited dopant (CuO), resulting in a lesser band gap energy [51]. Meanwhile, when fumed silica is applied as a support material (FS_Zn/Cu) the band gap energy is similar to the higher band gap material (FS_Zn), suggesting that the formation of the observed cluster in this sample affected the transition of the electrons generated from ZnO to CuO particles.

2.2. In Situ FTIR Characterisation

Additionally, acidic characteristics of studied samples were determined by **in situ *FTIR assays*** of pyridine adsorption and desorption under vacuum. Table 3 lists the concentration of Brønsted acid sites (BAS) and Lewis acid sites (LAS) of natural and modified zeolites as well as prepared single and double metal oxides supported on fumed silica. In this sense, after conducting the modification of natural zeolite by ion exchange with ammonium sulfate and thermally outgassed at 623 K (ZH sample), as it was expected, BAS concentration increased; meanwhile, LAS concentration diminished as compared to natural zeolite results. However, after the introduction of the copper and zinc oxides on previously modified zeolites, BAS were not detected by pyridine adsorption, and the amount of LAS is lower than in the other zeolite samples. Such results can be attributed to diffusion limitations of pyridine to access such acidic sites present in the natural zeolite and those created by ion exchange with ammonium, because of the blockage caused by the formation of aggregates of metal oxide nanoparticles or to dissolution and washing of the extra-framework phase during the process of metal introduction. Aggregates of metal oxide particles of bigger size can be responsible for the blockage of micropores, decreasing the catalyst surface area considerably, as shown in Table 1 [52].

Table 3. Characterization of the nature and strength of acidic surface sites of parent supports and prepared single and double metal oxide catalysts by in situ FTIR analyses using pyridine.

Samples	**Concentration of Brønsted Acidic Sites** [a] **[μmol *Py* g^{-1}]**	**Concentration of Lewis Acidic Sites** [a] **[μmol *Py* g^{-1}]**	**Strength Distribution of Lewis Acidic Sites (%)** [b]		
			Weak	**Mild**	**Strong**
ZNAT	17.21	84.69	49.47	9.08	41.45
ZH	78.00	37.00	0	0	100
ZH_Cu	ND	56.20	61.93	26.33	11.74
ZH_Zn	ND	34.20	43.10	4.59	52.31
ZH_Zn/Cu	ND	45.64	48.30	23.47	28.23
FS	ND	ND	ND	ND	ND
FS_Cu	ND	3.00	100	0	0
FS_Zn	ND	106.00	61.30	29.20	9.50
FS_Zn/Cu	ND	194.00	55.15	15.46	29.39

[a] Determined by in situ FTIR using pyridine as a probe molecule. [b] Determined by in situ FTIR after thermal-programmed desorption of adsorbed pyridine.

Finally, after the pyridine adsorption experiment, a temperature-programmed desorption was applied in order to obtain a rough estimate of the strength of the Lewis acidic sites. Results listed in Table 3 suggest that zinc sites enhance the Lewis acidity strength; whereas, copper presents the opposite trend in the modified zeolite samples. Moreover, the characterization of raw and modified fumed silica samples show a similar trend with an increased strength of LAS in the samples modified with zinc oxide. However, in this case, a higher LAS strength is observed when the double metal oxide catalyst was supported over the fumed silica (FS_ZnO/CuO).

2.3. Photocatalytic Oxidation of Ethylene onto Parent Zeolite Support and Prepared Single and Double Metal Oxide Catalysts Supported on Modified Natural Zeolite

The effect of the physical–chemical properties of the parent zeolite support and prepared single and double metal oxide catalysts supported on modified natural zeolite on the photocatalytic oxidation of ethylene are shown in Figures 5 and 6. Moreover, results of control experiments using pure raw fumed silica, prepared single and double metal oxide catalysts supported on fumed silica are also presented. Fumed silica consists of finely dispersed amorphous silicon dioxide with a surface covered by silanol groups [53]. Its use is widespread in industrial applications as a catalyst support and as an adsorbent [54,55]. Such kinds of experiments allow determination by comparison the role of acidic sites of zeolite surface in the photocatalytic reaction. Additionally, a benchmarked assay using TiO_2 P25 mixed with raw fumed silica is also displayed to contrast the photocatalytic performance of the composite materials under similar reaction conditions.

Curves of the ethylene dimensionless concentration at the reactor outlet stream as the function of time are displayed in Figure 5. The first 600 min of every curve represents the variation of ethylene dimensionless concentration during the adsorption step until saturation is reached (without irradiation). Adsorbed amounts of ethylene during the dynamic adsorption step onto the studied samples (μmol g^{-1}) are reported in Figure 6. Afterwards, the photocatalytic oxidation step takes place under irradiation conditions. As it can be seen, the stationary state of the photocatalytic step is attained after a few minutes. The photocatalytic removal of ethylene for each sample is also presented in Figure 6 and was calculated considering the concentration of ethylene in the reactor inlet and outlet streams in the stationary step.

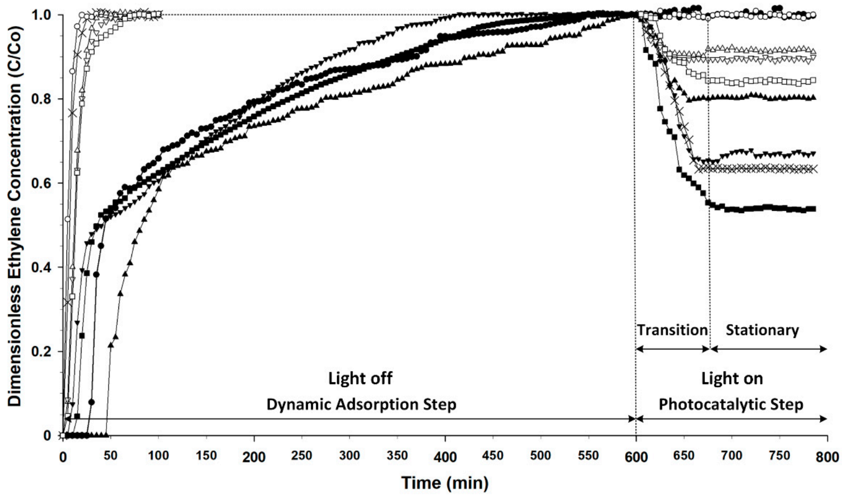

Figure 5. Ethylene adsorption and photocatalytic degradation using parent zeolite support. Prepared single and double metal oxide catalysts supported on modified natural zeolite, raw fumed silica, prepared single and double metal oxide catalysts supported on fumed silica, and TiO_2 mixed with raw fumed silica: ● ZNAT, ▲ ZH_Cu, ▼ ZH_Zn, ■ ZH_Zn/Cu, ○ FS, △ FS_Cu, ▽ FS_Zn, □ FS_Zn/Cu, X FS_TiO_2.

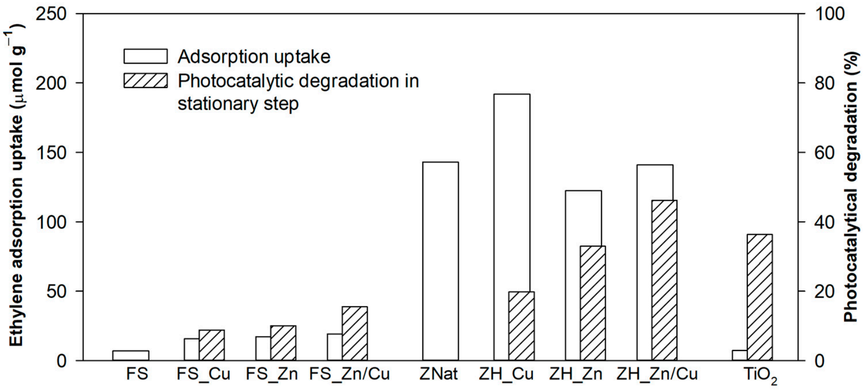

Figure 6. Ethylene adsorption and photocatalytic degradation results using parent zeolite support (ZNat), single metal oxide catalysts supported on modified natural zeolite (ZH_Cu; ZH_Zn), copper and zinc oxides supported on modified natural zeolite (ZH_Zn/Cu), raw fumed silica (FS), single metal oxide catalysts supported on fumed silica (FS_Cu; FS_Zn), and copper and zinc oxides supported on fumed silica (FS_Zn/Cu), and TiO_2 P25 mixed with fumed silica (FS_TiO_2).

Results displayed in Figures 5 and 6 provide evidence that the applied modification procedures slightly affect the adsorption capacity of natural zeolite and fumed silica toward ethylene molecules, mainly in those cases where samples are modified with copper salts. During the adsorption step, it can be observed that ethylene adsorption is almost negligible for raw and modified fumed silica samples compared to samples where zeolite is used as a support. Such differences could be related to the favorable physical–chemical surface properties of zeolite compared to fumed silica. The higher surface area, the presence of microporous and mesoporous structure with several Si-OH, and Si-OH-Al and cationic active sites contribute to the observed increase in the adsorption of ethylene in comparison to fumed silica. In the case of prepared single and double metal oxide catalysts supported on modified natural zeolite, the adsorption of ethylene during this step increases according to the following order: ZH_Zn_ < ZH_Zn/Cu < ZNat < ZH_Cu. Such results agree with those reported in a previous study [10]. Copper oxide supported on modified natural zeolite, leads to an enhancement in the adsorption capacity toward ethylene. The good dispersion of the copper oxides over the zeolite surface as reported in Figure 3C could favor its interaction with ethylene. Ethylene adsorption also takes place not only by the interaction with Si-OH-Al bridge groups of zeolite surface but also by the interactions between π-electrons of ethylene with metal cations deposited in the zeolite surface [5,10]. A lower adsorption of ethylene is obtained on ZH_Zn. Such a result could be related to (i) the observed formation of bigger aggregates of nanoparticles in this sample, as indicated by TEM images (see Figure 3D), (ii) the decrease in the surface area, as reported by N_2 adsorption assays (see Table 1), and (iii) the low accessibility to Brønsted and Lewis sites, as shown by pyridine adsorption (Table 3). The amount of adsorbed ethylene seems directly related to the surface area of the samples and to the surface concentration of Lewis sites.

Results displayed in Figure 6 confirm the good adsorption capacity of the modified natural zeolite used, as well as the single metal oxide catalysts supported on them. Some other ethylene adsorbents have been studied previously including activated carbon-based materials, carbon nanoballs, and synthetic and natural zeolites [7,9,12]. Such studies have reported ethylene adsorption capacities around 10 to 80 μmol g^{-1} [7] at similar ethylene concentrations. Regarding photocatalysis results, the highest degradation rate is achieved when the parent natural zeolite support is modified with both transition metal oxides (ZH_Zn/Cu). The single metal oxides supported on modified natural zeolite (ZH_Zn and ZH_Cu) are less active.

No photocatalytic oxidation is registered using the parent natural zeolite support (ZNat). A similar trend is attained during photocatalytic oxidation of ethylene using fumed silica as a support for metal oxides (FS_Zn/Cu > FS_Zn > FS_Cu > FS). No photodegradation is catalyzed by the raw fumed silica material (FS). Lower degradation values are obtained when the fumed silica is used as a support for metal oxides rather than the zeolite. In agreement with the stated working hypothesis, a higher photocatalytic degradation is accomplished with the double metal oxides supported on modified natural zeolite obtained by co-impregnation, being even higher than the benchmark TiO_2 sample. Such behaviors agree with those results obtained by UV-Vis spectroscopy characterization (see Figure 4). A higher degradation rate is reached in the sample that presents the highest UV light absorption as it is the case of ZH_Zn/Cu sample. Moreover, several studies have reported that ZnO possesses an excellent photocatalytic activity similar or even greater than that of TiO_2, in the degradation of organic compounds [30,32,33]. In addition, it was also reported that CuO presents a lower photocatalytic activity under UV irradiation than ZnO [56,57]. It is worth noting that the highest ethylene conversions are obtained when the catalysts based on both transition metal oxides are used, even when different materials are applied as supports.

In this heterostructure material zinc oxide could absorb UV photons, forming electron–hole (e–h) pairs, whereas copper oxide nanoparticles could reduce the recombination of e–h pairs, increasing the absorption of photons with lower energy [37]. It is well known that (e–h) pairs react with oxygen and water molecules, generating superoxide and hydroxyl radicals, respectively [22,42,58]. Such active species usually act as powerful oxidants, leading to the oxidation of close adsorbed ethylene molecules. Previous studies have reported the photocatalytic conversion of ethylene from 10 to 90% using TiO_2 based photocatalysts [7]. However, operational conditions were different from those applied in this study. It is worth noting that during photocatalytic oxidation processes, parameters such as wavelength irradiation, light intensity, catalyst load, among other factors could have an impact in the removal efficiency [59,60]. Thus, TiO_2 was used here as a benchmark photocatalyst as a way of comparison.

In addition, studies concerning other ethylene oxidation techniques such as $KMnO_4$ have shown almost full ethylene remotion at the first hours of use; however, it has a rapid loss of reaction efficiency during the time of storage [61]. Similarly, it has been mentioned that $KMnO_4$ can cause product contamination [62].

Moreover, the observed degradation rate in the single and double metal oxide catalysts supported on modified natural zeolite could have been favored by the presence of several adsorption sites where ethylene molecules are adsorbed and oxidized by the radicals generated in the nearby semiconductor oxide nanoparticles. More detailed information on such kinds of interactions is followed by *operando* DRIFTS studies and is presented in Figure 7.

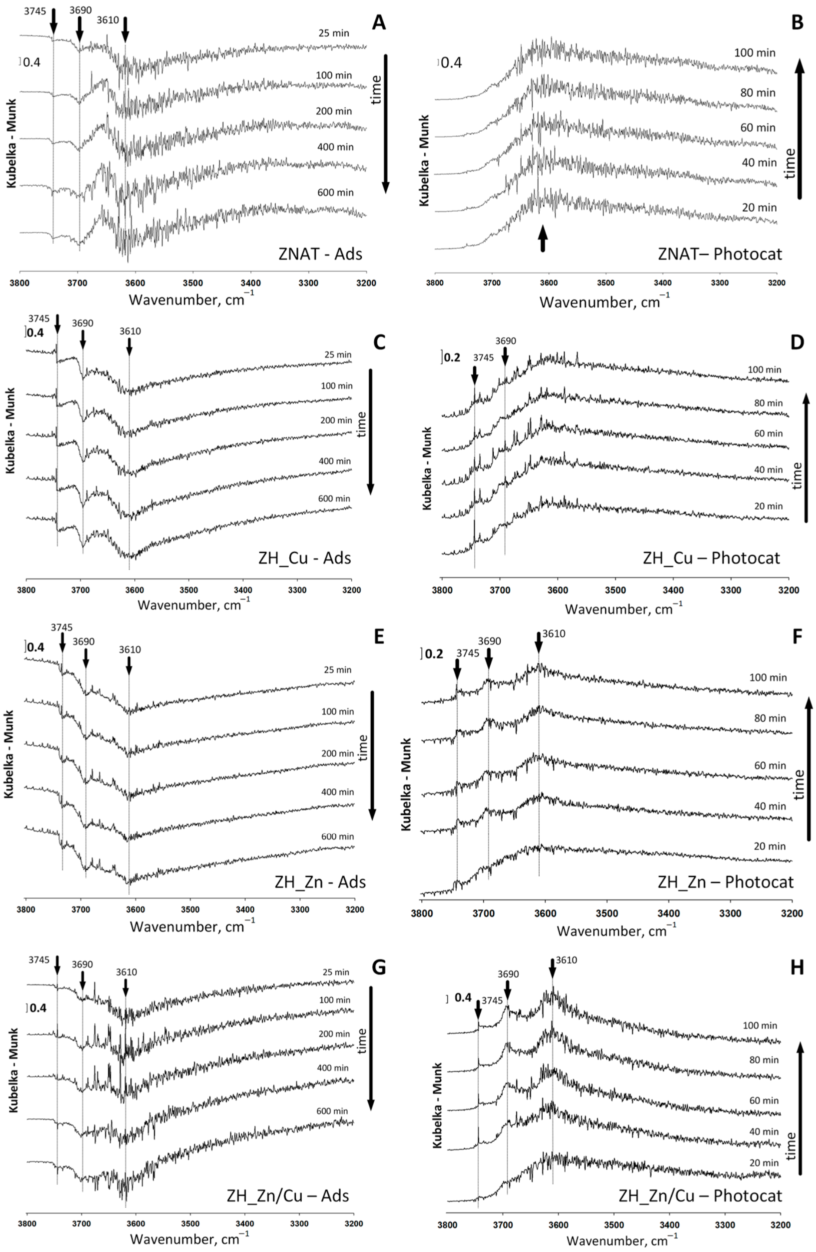

Figure 7. Evolution of subtracted DRIFTS spectra of the OH stretching vibration zone during the adsorption step (left) and photocatalytic degradation step of ethylene (right) onto parent zeolite support. Prepared single and double metal oxide catalysts supported on modified natural zeolite: ZNAT (**A**,**B**), ZH_Cu; (**C**,**D**); ZH_Zn (**E**,**F**); ZH_Zn/Cu; (**G**,**H**).

The variations of *operando* DRIFTS spectra during the adsorption step (without irradiation) of the experimental results presented in Figures 5 and 6 of ethylene onto single and double metal oxide catalysts supported on zeolite and fumed silica samples are shown in Figure 7A,C,E,G and Figure 8A,C,E,G, respectively. Additionally, *operando* DRIFTS spectra of TiO_2 interactions with ethylene through the adsorption step are also included in Figure 9A. Results displayed in Figures 7–9 represent the subtractions of the obtained spectrum for each sample as a function of ethylene exposition time and the respective spectrum of activated samples prior to ethylene contact. As was previously reported [10,63], in the ν(OH) region, between 4000 and 3300 cm^{-1}, the peak at 3745 cm^{-1} could be assigned to silanol groups (Si-OH) vibration. Moreover, the band at 3690 cm^{-1} comes from extra-framework phase, and the peak at 3610 cm^{-1} is the usual zeolitic Bronsted acidic OH group known as the bridge silanol (Si-OH-Al). The progressive loss on the intensities of the IR bands at 3590 cm^{-1}, 3690 cm^{-1}, and 3745 cm^{-1} related to OH groups are observed for the parent zeolite support, the prepared single and double metal oxide catalysts supported on modified natural zeolite. However, the higher difference is obtained at 3610 cm^{-1}, suggesting that most of ethylene adsorption occurs by the interaction with acidic Si-OH-Al groups. Although an increase in the adsorption of ethylene is observed for the zeolite samples modified with copper oxide (see Figure 6), no other IR vibrations are observed in the DRIFTS spectra beside those already mentioned during the adsorption step. This can be due to the low concentration of ethylene on the surface of the catalyst during the experiment and the fast decomposition and desorption in the photocatalytic step.

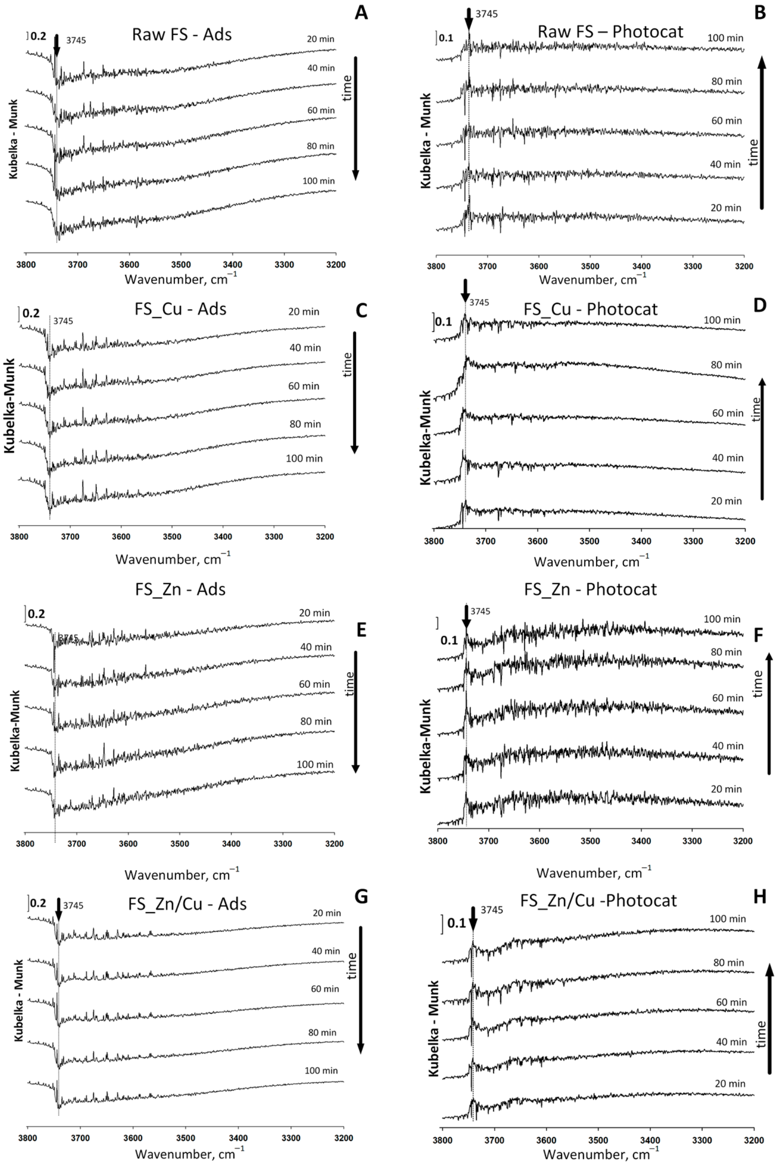

Figure 8. Evolution of subtracted DRIFTS spectra of the OH stretching vibration zone during the adsorption step (left) and photocatalytic degradation step of ethylene (right) onto raw fumed silica. Prepared single and double metal oxide catalysts supported on fumed silica: raw FS (**A**,**B**), FS_Cu (**C**,**D**), FS_Zn (**E**,**F**), and FS_Zn/Cu (**G**,**H**).

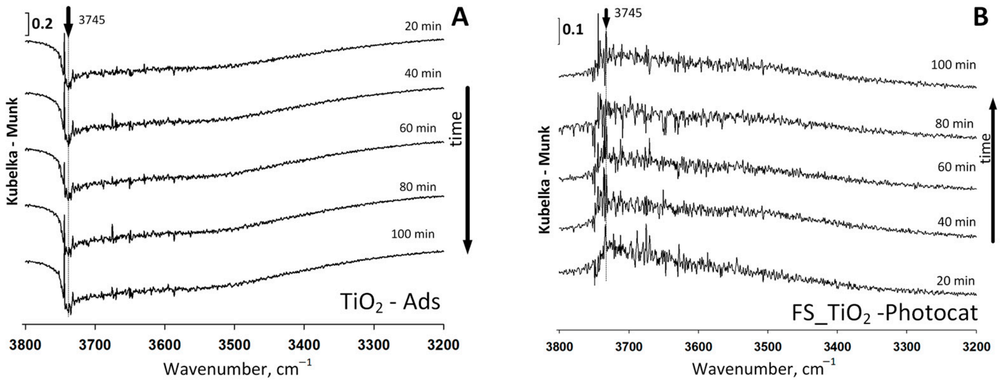

Figure 9. Evolution of subtracted DRIFTS spectra of the OH stretching vibration zone during the adsorption step (**A**) and photocatalytic degradation step of ethylene (**B**) onto TiO_2 mixed with raw fumed silica (FS_TiO_2).

In the case of the fumed silica sample (Figure 8A), recorded spectra show only intensity changes in the band located at 3745 cm^{-1} related to the presence of silanol groups in the raw material and its interaction with ethylene molecules during adsorption. Such sites are occupied quickly and remain invariable after the saturation is reached. A similar trend is observed for single and double metal oxide catalysts supported on fumed silica (Figure 8C,E,G) and for TiO_2 mixed with raw fumed silica at 8% of weight (Figure 9A). Such results agree with the almost negligible ethylene adsorption observed for these samples compared to zeolite supported catalysts with acidic Brønsted sites.

Spectra reported in Figures 7 and 8 are obtained at different time periods as subtraction of the registered spectra at specific times from the spectrum acquired when the saturation is reached at the final step of the adsorption stage of each sample. During the photocatalysis stage, as can be seen in Figure 7H, the ZH_Zn/Cu double catalyst show restored OH vibration bands (3745 cm^{-1}, 3690 cm^{-1}, and 3610 cm^{-1}) which had been consumed during the adsorption stage (see Figure 7G). Under irradiation, they are released again and became unoccupied due to the photocatalytic oxidation of adsorbed ethylene, leading to a new adsorption equilibrium. Analogous behavior can be observed on the single zinc oxide supported on modified natural zeolite (Figure 7F) and to a lesser extent, on the single copper oxide supported on modified natural zeolite (Figure 7D). Ethylene molecules adsorbed in such sites could be oxidized by radicals generated at nanoparticles of copper and zinc oxides. Hence, some recovered adsorption sites allow new ethylene molecules to be adsorbed and oxidized photocatalytically. However, in the case of the parent zeolite support, subtracted DRIFTS spectra (Figure 7B) do not show any evolution in the vibration of OH characteristic bands during the experiment, suggesting that in the absence of the semiconductor particles, ethylene cannot be eliminated. Such results agree with those obtained by monitoring the concentration of ethylene at the inlet and outlet stream of the photocatalytic reaction cell using GC analyses (see Figures 5 and 6). The double metal oxide catalyst based on copper and zinc oxides supported on modified natural zeolite shows the highest removal efficiency toward ethylene oxidation in the series, and the parent natural zeolite support (ZNAT) does not show any C_2H_4 removal.

Operando DRIFTS assays during the photocatalytic step with fumed silica samples confirm that there is no contribution of the raw fumed silica during the photocatalytic oxidation step and are shown in the supplementary materials. In the other fumed silica samples, a slight change can be perceived in the IR band at 3745 cm^{-1}, but only at the beginning of the irradiation, It cannot be attributed to photocatalytic oxidation, but rather, just to the effect of heating during this short transition period that leads to a fast elimination of the few ethylene adsorbed in these samples. Afterwards, in the stationary state, the surface of those samples remains unchanged.

Similar changes in the OH bands were observed when TiO_2 mixed with raw fumed silica was used (Figure 9). The spectra of such sample showed only the disappearance of the IR vibration band at 3745 cm^{-1} related to OH groups during the adsorption step. The same signal came back after the photocatalytic step, indicating less adsorption sites for ethylene compared to samples containing modified zeolite.

Results obtained here account for different factors that are involved during the photocatalytic oxidation of ethylene. When metal oxide semiconductors are deposited in a support with almost negligible adsorption capacity, as with fumed silica compared to zeolite, ethylene oxidation efficiencies are below 20% (see Figures 5 and 6). The observed outcomes suggest that zinc oxide is mainly responsible for photocatalytic degradation. When zinc oxide is combined with copper oxide, a material with higher photocatalytic activity is obtained. Other researchers similarly reported that in heterostructure catalysts, where zinc and copper oxides are combined, the electron–hole pair separation efficiency is enhanced, increasing the photocatalytic activity [37,58,64]. However, when metal oxide semiconductors are deposited over a material with a high adsorption capacity, such as modified natural zeolite, the retention of ethylene molecules at adsorption sites in the vicinity of semiconductor particles could be the main factor for the observed increase in the overall oxidation efficiency. The DRIFTS assay of the ZH_Zn/Cu sample provides evidence that adsorbed ethylene molecules at acidic surface sites are photocatalytically removed once the semiconductors are irradiated. In this way, the oxidation ability of superoxide and hydroxyl radicals generated due to the e–h pairs activation and their interactions with oxygen and water molecules could be more efficient when the semiconductor materials are supported over a material with high content of acidic surface sites that allow radicals to oxidize ethylene molecules adsorbed in their vicinity.

2.4. Mechanistic Approach

Results reported here in addition to previous studies [10] contribute to validate the hypothesis of ethylene elimination by a synergic mechanism that includes adsorption and photocatalytic oxidation. DRIFTS analyses enable to track acidic groups of zeolite surface and their behavior during the process. The use of modified natural zeolite as a support for zinc and copper oxides allows ethylene to be mainly adsorbed at bridged hydroxyl and at external and internal silanol sites as it is represented by Equation (1). Moreover, in hydrophilic zeolites such as the natural zeolite used here, water molecules also interact mainly with bridged hydroxyl groups affiliated mainly with aluminum in the zeolite lattice (Equation (2)).

$$\mathrm{C_2H_4 + * \leftrightarrow C_2H_4*} \tag{1}$$

$$\mathrm{H_2O + *BAS \leftrightarrow H_2O*BAS} \tag{2}$$

Under irradiation, zinc and copper oxides seem to absorb UV photons, forming electron–hole (e–h) pairs (Equation (3)).

$$\mathrm{ZnO/CuO} + hv \rightarrow \mathrm{n}\left(\mathrm{h^+ + e^-}\right) \tag{3}$$

In the nanoparticles of semiconductors, zinc oxide increases the optical absorption; whereas, copper oxide nanoparticles decrease the optical band gap of the material, increasing the absorption of photons with lower energy and reducing the e–h recombination rate [65–68]. It is generally accepted that generated electrons and electrons' holes interact with oxygen and water molecules, producing superoxide and hydroxyl radicals [60] (Equations (4)–(8)) increasing the efficiency of the photocatalytic process [60,69,70].

$$\mathrm{h^+ + H_2O* \rightarrow O\mathring{H} * + H^+} \tag{4}$$

$$\mathrm{e^- + O_2 \rightarrow O_2^{-\circ}} \tag{5}$$

$$\mathrm{O_2^{-\circ} + H^+ \rightarrow H\mathring{O}_2} \tag{6}$$

$$\mathrm{H^+ + O_2^{-\circ} + H\mathring{O}_2 \rightarrow H_2O_2 + O_2} \tag{7}$$

$$H_2O_2 + h\upsilon \rightarrow 2OH^{\circ} \tag{8}$$

Finally, such radical species seems to be the responsibility of photocatalytic degradation of adsorbed ethylene at the neighboring site, generating intermediary oxidation by-products [60] (Equations (9)–(10)) that finally lead to ethylene mineralization, as summarized by Equation (11).

$$OH^{\circ} * + C_2H_4* \rightarrow \text{Intermediates} \tag{9}$$

$$O_2^{-\circ} + C_2H_4* \rightarrow \text{Intermediates} \tag{10}$$

$$C_2H_4 + 3O_2 \xrightarrow[cat]{h\nu} 2CO_2 + 2H_2O \tag{11}$$

Comparative experiments conducted using fumed silica as a support with poor adsorption capacity towards ethylene proved the important role of acidic surface sites of zeolite, increasing the adsorption of ethylene and its photocatalytic oxidation in the vicinity of zinc and copper oxides. Further experiments are needed in order to unveil the details of the formation of intermediary oxidation by-products of higher molecular mass than water and CO_2. Dynamic studies of ethylene photocatalysis presented here were conducted in a continuous packed bed cell set in a FT/IR spectrometer using only one initial ethylene concentration in order to compare the catalysts' activity. For the purpose to gather kinetic information, further extensive experimentation must be conducted using ethylene at different initial concentrations.

3. Materials and Methods

3.1. Materials and Reagents

A natural zeolite (53% clinoptilolite, 40% mordenite, and 7% quartz) was used in this study as a parent support material and was provided by the Chilean mining company "Minera Formas". Ethylene (0.01% in Ar) was supplied by Indura (Santiago, Chile), whereas argon (>99.9% purity) and oxygen (>99.5% purity) were supplied by Praxair (Santiago, Chile). Inorganic chemicals (>99.5% purity) such as $(NH_4)_2SO_4$ and $Cu(NO_3)_2{\cdot}3H_2O$ were purchased from Merck (Darmstadt, Germany). $Zn(NO_3)_2{\cdot}6H_2O$ was supplied by Sigma-Aldrich Corporation (St. Louis, MO, USA). Solutions were prepared using deionized water ($\geq$18.0 MΩ cm) produced in a Thermo Scientific Barnstead Easypure II RF system (Thermo Fisher Scientific, Waltham, MA, USA).

3.2. Modification of Parent Support

Natural zeolite modification was carried out in consecutive stages. First, raw material was ground and sieved to a range of 300–425 µm particle size. Then, it was rinsed with deionized water and dried at 398 K for 24 h, using a LabTech® oven model LDO-080F (Daihan LabTech Co., Ltd., Gyeonggi-do, Korea).

In the pre-treatment stage, raw zeolite was modified by ion exchange with ammonium sulphate (0.1 mol dm^{-3}) at 363 K for two hours in a temperature-controlled water bath, using a mass volume ratio of 0.1 g of zeolite per cm^3 of salt solution and then it was washed with deionized water during 4 h to eliminate the excess of salt as it has been reported in previous work [10]. This procedure was repeated once after rinsing. Samples were dried at 398 K for 24 h. Afterwards, samples were out-gassed at 623 K using a home-made tubular furnace (heating rate of 3 K min^{-1}) during two hours under argon flow (100 cm^3 min^{-1}).

During the metal loading stage, pre-treated samples were modified by wet impregnation using an IKA® RV 10 vacuum rotary evaporator (IKA®-Werke, Staufen, Germany) at 363 K. Thus, two single metal oxide and one double metal oxide catalysts were obtained by single impregnation with $Cu(NO_3)_2{\cdot}3(H_2O)$ (0.13 mol dm^{-3}), single impregnation with $Zn(NO_3)_2{\cdot}6(H_2O)$ (0.13 mol dm^{-3}), and co-impregnation using a combination of both salts at 0.065 mol dm^{-3}, respectively. Salt solution concentrations were calculated to obtain single metal oxide catalysts with 8% of the desired metal oxide mass impregnated in the zeolite surface and a double metal oxide catalyst with 4% of each metal oxide in the co-impregnated sample. Subsequently, samples were dried using the same conditions mentioned before. As the last modification step, samples were calcined under oxygen flow (100 cm^3 min^{-1}) at 623 K (heating rate of 1 K min^{-1}) for 4 h and stored in a desiccator until their further use. Additionally, fumed silica was used as a support of metal oxides in control experiments. Raw fumed silica was modified using the same sequential procedure described before for the metal loading stage, including the followed modification steps. The performance of the samples prepared using natural zeolite and fumed silica were compared to understand the key role of acidic sites of zeolite surface in the photocatalytic process.

According to the applied modification methodology, samples were named as follows:

- Natural zeolite thermally outgassed at 623 K (ZNAT);
- H form of natural zeolite (ZH), obtained from natural zeolite modified by ion exchanged with ammonium and thermally outgassed at 623 K;
- Copper oxide supported on modified natural zeolite, obtained from natural zeolite ion exchanged with ammonium followed by a single wet impregnation with copper salt and later calcined at 623 K (ZH_Cu);
- Zinc oxide supported on modified natural zeolite, obtained from natural zeolite ion exchanged with ammonium followed by a single wet impregnation with zinc salt and later calcined at 623 K (ZH_Zn);
- Copper and zinc oxides supported on modified natural zeolite, obtained from natural zeolite ion exchanged with ammonium followed by a wet co-impregnation with copper and zinc salts and later calcined at 623 K (ZH_Zn/Cu);
- Raw fumed silica thermally outgassed at 623 K (FS);
- Copper oxide supported on fumed silica, obtained from fumed silica modified by single wet impregnation with copper salt and later calcined at 623 K (FS_Cu);
- Zinc oxide supported on fumed silica, obtained from fumed silica modified by single wet impregnation with zinc salt and later calcined at 623 K (FS_Zn);
- Copper and zinc oxides supported on fumed silica, obtained from fumed silica modified by wet co-impregnation with copper and zinc salts and later calcined at 623 K (FS_Zn/Cu).

Furthermore, TiO_2 (99.9% purity) supplied by Evonik (Nuremberg, Germany) was mixed with the raw fumed silica at 8% weight and thermally outgassed at 623 K and used as a benchmark catalyst for comparison (FS_TiO_2).

3.3. Characterisation of the Parent Zeolite Support and of the Single and Double Metal Oxide Catalysts

The parent zeolite support and the single and double metal oxide catalysts supported on modified natural zeolite were characterized using different analytical techniques. X-ray powder diffraction (XRD) patterns were obtained using a Bruker Endeavor diffractometer model D4/MAX-B with a copper cathode lamp (λ = 1.541 Å), operated at 20 mA and 40 kV. X-ray diffraction patterns were collected with a 0.02° resolution from 4° to 80° and a time interval of 1 s. The specific surface areas were determined by nitrogen adsorption at 77 K, using Micromeritics ASAP 2000 equipment (Norcross, GA, USA). Samples were previously outgassed at 623 K during 2 h under inert flow (70% N_2, 30% He). The surface area values were determined using the single-point surface area method, as described elsewhere [71]. The chemical composition of the parent zeolite support, single and double metal oxide catalysts supported on modified natural zeolite were determined by X-ray fluorescence (XRF) using a Rigaku model ZSX Primus II spectrometer. Scanning electron microscopy (SEM) images were obtained in a Mira L.M.H. microscope operated at 30 kV and 177 µA. Samples were ground, deposited over a carbon film, and covered with a platinum coat. A high vacuum ($<3 \times 10^{-4}$ mbar) was established in the microscope before image acquisition. Transmission electron microscopy (TEM) studies were carried out in a JEOL, JEM 1200 EX-II device equipped with a Gatan 782 camera and using an accelerating voltage of 120 kV. Samples were ground and deposited over a carbon covered mesh for imagery.

In situ IR assays of pyridine adsorption under vacuum were conducted to determine the concentration and strength of acidic sites present in the parent supports and in the prepared single and double metal oxide catalysts. Pyridine interactions with Brønsted and Lewis acid sites were monitored by Fourier transform infrared spectroscopy (FTIR). Samples were ground to powder and compacted as self-supported pellets of 20 mg and 16 mm diameter. Pellets were heated inside a thermo-regulated FTIR glass cell to 623 K (heating rate of 3 K min^{-1}) and activated under high vacuum ($<7 \times 10^{-5}$ mbar) for 12 h. Pyridine adsorption experiments were carried out at 423 K in a Nicolet 5700 spectrometer (Thermo Fisher Scientific Inc., Waltham, MA, USA) equipped with an MCT/A detector. Spectra were averaged from 32 consecutive acquisitions obtained in the range from 4000–1100 cm^{-1} with a resolution of 4 cm^{-1}, using the OMNIC software V 9.2.86. After adsorption experiments, thermal-programmed desorption of pyridine was performed under vacuum. FTIR spectra were collected after heating the pyridine saturated samples from 463 K to 723 K to study strength of acidic sites. Thus, the percentage of pyridine desorbed at different temperature ranges from 463 K to 523 K, from 523 K to 623 K, and from 623 K to 723 K are related to weak, mild, and strong acidic sites, respectively [72].

The amount of Brønsted acid sites (BAS) and Lewis acid sites (LAS), expressed in terms of µmol of adsorbed pyridine per gram of catalyst, were determined from the integrated intensity of the absorption bands at 1545 cm^{-1} and at 1445–1450 cm^{-1}, respectively, using the commonly used modified Beer–Lambert–Bouguer law (Equation (12)):

$$A = \varepsilon \frac{n^{Py}}{S} \tag{12}$$

where n^{Py} is the number of Py species (in µmol) adsorbed at the acidic site (Lewis or Brønsted), A is the peak area (in cm^{-1}), and S is the cross-section area of the zeolite disc (S = 2 cm^2). ε is the integrated molar absorption coefficient (in cm µmol^{-1}). The values for ε were taken from the work of Zholobenko et al. [73], as 1.38 and 1.87 cm µmol^{-1} for Brønsted and Lewis acid sites, respectively, in mordenites.

UV-visible light absorption properties of the prepared photo-catalysts were assessed by UV-Vis DRS spectroscopy. Experiments were carried out in a VARIAN 4000 UV-Vis spectrophotometer equipped with an integration sphere. Solid samples were located in the sample holder and spectra were collected in the range from 200–800 nm in absorbance mode. The optical band gap energy was determined applying the Tauc Plot methodology by extrapolating the linear part of the vertical region of the curve [41,51].

3.4. Photocatalytic Degradation of Ethylene

Photocatalytic experiments were conducted in a commercial Praying Mantis$^{\mathrm{TM}}$ DRIFTS cell (Harrick Scientific, New York, NY, USA) containing a quartz window and set in a JASCO FT/IR 4700 spectrometer equipped with an MCT/M detector (JASCO International Co., Ltd., Tokyo, Japan). Dynamic photocatalytic experiments were performed using 0.08 g of sample deposited in the DRIFTS chamber. Prior to any experiment, zeolite samples were activated for 2 h at 623 K (heating rate of 1 K min^{-1}) under vacuum. Irradiation during photo-catalytic experiments was supplied by a polychromatic light emitted by an LC8 spot light source (L10852, 200 W) from Hamamatsu Photonics (Shizuoka, Japan). A light guide from Hamamatsu was placed in the quartz window of the Praying Mantis DRIFTS cell. The irradiation intensity was measured using a light power meter from Hamamatsu Photonics (Shizuoka, Japan). The experimental setup used in this study (see Figure 10) was adapted from one used previously [10].

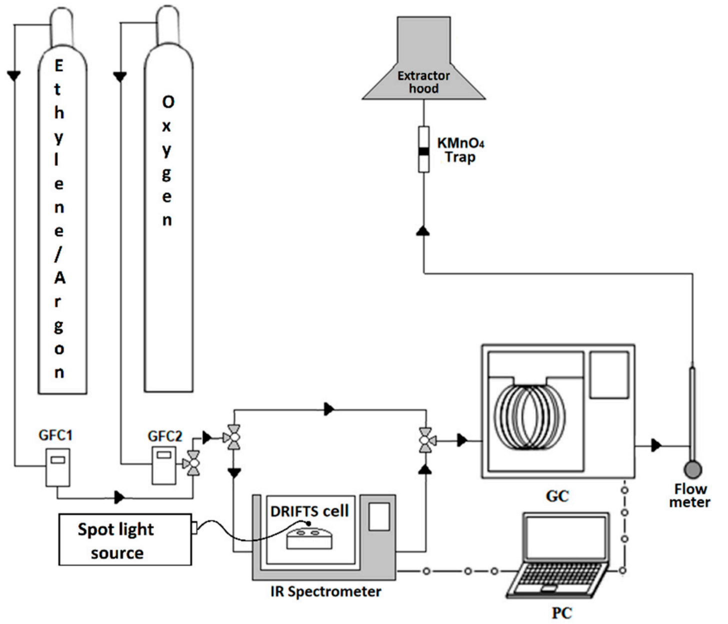

Figure 10. Schematic representation of the experimental set-up used for photocatalytic oxidation of ethylene.

In a typical experiment, a total flow of 25 cm^3 min^{-1} of a gas mixture composed of 80 ppmv of C_2H_4 and 20,000 ppmv of O_2 balanced in argon was continuously supplied over the sample bed (simulating the atmosphere around stored fruits). For each sample, an adsorption step was initially conducted with the light turned off until saturation was reached. Once the ethylene saturation was achieved, the light was turned on and the photocatalytic step was initiated. The temperature of the photocatalytic reactor cell was kept constant at 293 K, using a water jacketed heat exchanger. During the whole experimentation, spectra were collected as a function of time in the range of 4000–400 cm^{-1} with a resolution of 1 cm^{-1} using the spectra manager software V 2.14.02 (JASCO International Co., Ltd., Tokyo, Japan). At the same time, the concentrations of ethylene and CO_2 at the reactor outlet were monitored on-line by gas chromatography (Perkin Elmer Clarus 500 gas chromatographer, Waltham, MA, USA) using a flame ionization detector (FID) and a thermal conductivity detector (TCD), respectively. More detailed information about analytic techniques can be found elsewhere [10].

Adsorption capacities obtained during the first step (with the light turned off) toward ethylene using the parent zeolite support. The prepared single and double metal oxide catalysts supported on modified natural zeolite and fumed silica were determined by the integration of the breakthrough curves until reaching saturation conditions (Equation (13)), as follows:

$$q_{ethylene} = \frac{FC_{in}}{m} \int_0^{t_s} \left(1 - \frac{C_{out}}{C_{in}}\right) dt \tag{13}$$

where $q_{ethylene}$ ($\mu mol_{ethylene}$ g^{-1}) represents the total amount of ethylene adsorbed per gram of sample, F (cm^3 min^{-1}) stands for the gas flow rate, m (g) is the mass of sample inside the DRIFTS cell, t_s (min) is the adsorption time to reach saturation, C_{in} and C_{out} (μmol dm^{-3}) are the inlet and outlet concentrations of ethylene as a function of time, respectively.

The percentage of photocatalytic removal of ethylene obtained during the second step (with the light turned on) was calculated from experiments at steady state conditions, taking into consideration the amount of ethylene in the reactor inlet and outlet streams.

4. Conclusions

Modified natural zeolites could be used as support for copper and zinc oxides leading to efficient photocatalytic oxidation of ethylene. DRIFTS results evidenced a synergistic effect of adsorption and photocatalytic oxidation over the catalyst surface. Among the functional groups of zeolite surface, acidic Al-OH-Si bridges are the most influential for ethylene adsorption. Such surface groups concentrate ethylene molecules near to the photocatalyst semiconductor nanoparticles of zinc and copper oxides that promote ethylene oxidation under light irradiation. A photocatalyst based on nanoparticles of zinc and copper oxides supported o modified natural zeolite provides the highest contribution to photocatalytic activity toward ethylene oxidation. The increase in light absorption combined with a reduction in the band gap energy contributes to an enhancement in the photocatalytic oxidation of adsorbed ethylene. The development of new composite materials comprising semiconductors supported over zeolite for photocatalytic oxidation of ethylene emissions from fruit warehouses ought to consider the chemical surface interactions among the combined materials and ethylene. Moreover, further experiments should be performed using a light source with a wavelength corresponding to visible spectra in order to prove that better photocatalytic efficiencies are obtained using zeolites modified with copper and zinc oxide nanoparticles that take the advantage of the visible spectrum of solar radiation.

Supplementary Materials: The following supporting information can be downloaded at: https://www.mdpi.com/article/10.3390/catal13030610/s1, Figure S1: Nitrogen adsorption/desorption isotherms at 77 K of parent zeolite support and prepared single and double metal oxide catalysts supported on modified natural zeolite, Figure S2: Nitrogen adsorption/desorption isotherms at 77 K of fumed silica support and prepared single and double metal oxide catalysts supported on fumed silica.

Author Contributions: Conceptualization, N.J.A., H.V., F.A.-J. and C.A.Z.; methodology, N.J.A., H.V., F.A.-J. and T.F.d.O.; formal analysis, N.J.A., H.V. and C.A.Z.; investigation, N.J.A. and H.V.; resources, N.J.A., F.A.-J. and H.V.; data curation, N.J.A.; writing—original draft preparation, N.J.A. and H.V.; writing—review and editing, N.J.A., H.V. and F.T.-S.; visualization, N.J.A., H.V., T.F.d.O. and F.A.-J.; supervision, H.V.; project administration, H.V.; funding acquisition, H.V. and N.J.A. All authors have read and agreed to the published version of the manuscript.

Funding: This research was funded by CONICYT, FONDECYT/Regular (Grant 1170694); ANID, FONDECYT/postdoctorate (Grant 3210158) and CONICYT, PCHA/Doctorado Nacional 2015 (Grant 21150082).

Informed Consent Statement: Not applicable.

Data Availability Statement: Data are contained within the article tables and supplementary material.

Acknowledgments: The authors are grateful to the SMARTC Center from Scientific and Technological Bioresources Nucleus for their collaboration with assays and imagery. The authors also want to thank Mohamad El-Roz from *CNRS Laboratoire Catalyse et Spectrochimie* for his helpful discussion and Víctor A. Solar from *Laboratorio de Tecnologías Limpias*, *Universidad Católica de la Santísima Concepción* for his valuable collaboration.

Conflicts of Interest: The authors declare no conflict of interest.

References

1. Iqbal, N.; Khan, N.A.; Ferrante, A.; Trivellini, A.; Francini, A.; Khan, M.I.R. Ethylene role in plant growth, development and senescence: Interaction with other phytohormones. *Front. Plant Sci.* **2017**, *8*, 475. [CrossRef]
2. Aprianti, S.; Bintoro, N. The effect of concentrations and exposure durations of ethylene gas on the respiration rate of tomato fruit (*Solanum lycopersicum*). *IOP Conf. Ser. Earth Environ. Sci.* **2021**, *653*, 012021. [CrossRef]
3. Blanke, M. Challenges of Reducing Fresh Produce Waste in Europe—From Farm to Fork. *Agriculture* **2015**, *5*, 389–399. [CrossRef]
4. Blanke, M.M.; Shekarriz, R. Ethylene levels along the food supply chain—A key to reducing food waste? *Acta Hortic.* **2015**, *1091*, 101–106. [CrossRef]
5. Saltveit, M.E. Effect of ethylene on quality of fresh fruits and vegetables. *Postharvest Biol. Technol.* **2021**, *15*, 279–292. [CrossRef]
6. Kader, A.A.; Cavalieri, R.; Ferguson, I. A Perspective on Postharvest Horticulture (1978–2003). *Hortscience* **2006**, *38*, 1004–1008. [CrossRef]
7. Keller, N.; Ducamp, M.N.; Robert, D.; Keller, V. Ethylene removal and fresh product storage: A challenge at the frontiers of chemistry. Toward an approach by photocatalytic oxidation. *Chem. Rev.* **2013**, *113*, 5029–5070. [CrossRef] [PubMed]

8. Kim, S.I.; Aida, T.; Niiyama, H. Binary adsorption of very low concentration ethylene and water vapor on mordenites and desorption by microwave heating. *Sep. Purif. Technol.* **2005**, *45*, 174–182. [CrossRef]
9. Erdoğan, B.; Sakizci, M.; Yörükoğullari, E. Characterization and ethylene adsorption of natural and modified clinoptilolites. *Appl. Surf. Sci.* **2008**, *254*, 2450–2457. [CrossRef]
10. Abreu, N.J.; Valdés, H.; Zaror, C.A.; Azzolina-Jury, F.; Meléndrez, M.F. Ethylene adsorption onto natural and transition metal modified Chilean zeolite: An operando DRIFTS approach. *Microporous Mesoporous Mater.* **2019**, *274*, 138–148. [CrossRef]
11. Golipour, H.; Mokhtarani, B.; Mafi, M.; Moradi, A.; Godini, H.R. Experimental Measurement for Adsorption of Ethylene and Ethane Gases on Copper-Exchanged Zeolites 13X and 5A. *J. Chem. Eng. Data* **2020**, *65*, 3920–3932. [CrossRef]
12. Cisneros, L.; Gao, F.; Corma, A. Silver nanocluster in zeolites. Adsorption of ethylene traces for fruit preservation. *Microporous Mesoporous Mater.* **2019**, *283*, 25–30. [CrossRef]
13. Van Zandvoort, I.; van Klink, G.P.M.; de Jong, E.; van der Waal, J.C. Selectivity and stability of zeolites [Ca]A and [Ag]A towards ethylene adsorption and desorption from complex gas mixtures. *Microporous Mesoporous Mater.* **2018**, *263*, 142–149. [CrossRef]
14. Guo, Y.; Zu, B. Zeolite-based Photocatalysts: A Promising Strategy for Efficient Photocatalysis. *J. Thermodyn. Catal.* **2013**, *4*, e120. [CrossRef]
15. Bahrami, M.; Nezamzadeh-Ejhieh, A. Effect of the supported ZnO on clinoptilolite nano-particles in the photodecolorization of semi-real sample bromothymol blue aqueous solution. *Mater. Sci. Semicond. Process.* **2015**, *30*, 275–284. [CrossRef]
16. Erdoğan, B. A comparative adsorption study of C_2H_4 and SO_2 on clinoptilolite-rich tuff: Effect of acid treatment. *J. Hazard. Mater.* **2013**, *262*, 627–633. [CrossRef]
17. Sue-aok, N.; Srithanratana, T.; Rangsriwatananon, K.; Hengrasmee, S. Study of ethylene adsorption on zeolite NaY modified with group I metal ions. *Appl. Surf. Sci.* **2010**, *256*, 3997–4002. [CrossRef]
18. Kuz'min, I.V.; Sokolova, N.A.; Subbotina, I.R.; Zhidomirov, G.M. Ethylene adsorption and transformation on zeolite Ga^+/ZSM5. *Russ. Chem. Bull.* **2015**, *64*, 278–283. [CrossRef]
19. Despres, J.; Koebel, M.; Kröcher, O.; Elsener, M.; Wokaun, A. Adsorption and desorption of NO and NO_2 on Cu-ZSM-5. *Microporous Mesoporous Mater.* **2003**, *58*, 175–183. [CrossRef]
20. Phanichphant, S.; Nakaruk, A.; Chansaenpak, K.; Channei, D. Evaluating the photocatalytic efficiency of the $BiVO_4$/rGO photocatalyst. *Sci. Rep.* **2019**, *9*, 16091. [CrossRef]
21. Li, R.; Li, T.; Zhou, Q. Impact of titanium dioxide (TiO_2) modification on its application to pollution treatment—A review. *Catalysts* **2020**, *10*, 804. [CrossRef]
22. El-Roz, M.; Bazin, P.; Daturi, M.; Thibault-Starzyk, F. On the mechanism of methanol photooxidation to methylformate and carbon dioxide on TiO_2: An operando-FTIR study. *Phys. Chem. Chem. Phys.* **2015**, *17*, 11277–11283. [CrossRef]
23. Kozlov, D. Titanium dioxide in gas-phase photocatalytic oxidation of aromatic and heteroatom organic substances: Deactivation and reactivation of photocatalyst. *Theor. Exp. Chem.* **2014**, *50*, 133–154. [CrossRef]
24. Abbas, N.; Hussain, M.; Russo, N.; Saracco, G. Studies on the activity and deactivation of novel optimized TiO_2 nanoparticles for the abatement of VOCs. *Chem. Eng. J.* **2011**, *175*, 330–340. [CrossRef]
25. Shao, M.; Chen, W.; Ding, S.; Lo, K.H.; Zhong, X.; Yao, L.; Ip, W.F.; Xu, B.; Wang, X.; Pan, H. WX_y/G-C_3N_4 ($WX_y = W_2C$, WS_2, or W_2N) Composites for Highly Efficient Photocatalytic Water Splitting. *ChemSusChem* **2019**, *12*, 3355–3362. [CrossRef] [PubMed]
26. Mera, A.C.; Rodriguez, C.A.; Pizarro-Castillo, L.; Melendrez, M.F.; Valdés, H. Effect of Temperature and Reaction Time during Solvothermal Synthesis of BiOCl on Microspheres Formation: Implications in the Photocatalytic Oxidation of Gallic Acid under Simulated Solar Radiation. *J. Sol-Gel. Sci. Technol.* **2020**, *95*, 146–156. [CrossRef]
27. Li, D.; Haneda, H. Morphologies of Zinc Oxide Particles and Their Effects on Photocatalysis. *Chemosphere* **2003**, *51*, 129–137. [CrossRef]
28. Al-Ariki, S.; Yahya, N.A.A.; Al-A'nsi, S.A.; Jumali, M.H.H.; Jannah, A.N.; Abd-Shukor, R. Synthesis and comparative study on the structural and optical properties of ZnO doped with Ni and Ag nanopowders fabricated by sol gel technique. *Sci. Rep.* **2021**, *11*, 11948. [CrossRef]
29. Ayoub, I.; Kumar, V.; Abolhassani, R.; Sehgal, R.; Sharma, V.; Sehgal, R.; Swart, H.C.; Mishra, Y.K. Advances in ZnO: Manipulation of defects for enhancing their technological potentials. *Nanotechnol. Rev.* **2022**, *11*, 575–619. [CrossRef]
30. Hanif, M.A.; Kim, Y.S.; Ameen, S.; Kim, H.G.; Kwac, L.K. Boosting the Visible Light Photocatalytic Activity of ZnO through the Incorporation of N-Doped for Wastewater Treatment. *Coatings* **2022**, *12*, 579. [CrossRef]
31. Adeel, M.; Saeed, M.; Khan, I.; Muneer, M.; Akram, N. Synthesis and characterization of Co–ZnO and evaluation of its photocatalytic activity for photodegradation of methyl orange. *ACS Omega* **2021**, *6*, 1426–1435. [CrossRef]
32. Ma, S.; Huang, Y.; Hong, R.; Lu, X.; Li, J.; Zheng, Y. Enhancing Photocatalytic Activity of ZnO Nanoparticles in a Circulating Fluidized Bed with Plasma Jets. *Catalysts* **2021**, *11*, 77. [CrossRef]
33. Mao, T.; Liu, M.; Lin, L.; Cheng, Y.; Fang, C. A Study on Doping and Compound of Zinc Oxide Photocatalysts. *Polymers* **2022**, *14*, 4484. [CrossRef]
34. Modwi, A.; Ghanem, M.A.; Al-Mayouf, A.M.; Houas, A. Lowering energy band gap and enhancing photocatalytic properties of Cu/ZnO composite decorated by transition metals. *J. Mol. Struct.* **2018**, *1173*, 1–6. [CrossRef]
35. Dhineshbabu, N.R.; Rajendran, V.; Nithyavathy, N.; Vetumperumal, R. Study of structural and optical properties of cupric oxide nanoparticles. *Appl. Nanosci.* **2016**, *6*, 933–939. [CrossRef]

36. Bekru, A.G.; Tufa, L.T.; Zelekew, O.A.; Goddati, M.; Lee, J.; Sabir, F.K. Green Synthesis of a CuO-ZnO Nanocomposite for Efficient Photodegradation of Methylene Blue and Reduction of 4-Nitrophenol. *ACS Omega* **2022**, *7*, 30908–30919. [CrossRef]
37. Wei, A.; Xiong, L.; Sun, L.; Liu, Y.J.; Li, W.W. CuO nanoparticle modified ZnO nanorods with improved photocatalytic activity. *Chin. Phys. Lett.* **2013**, *30*, 046202. [CrossRef]
38. Maraj, M.; Raza, A.; Wang, X.; Chen, J.; Riaz, K.N.; Sun, W. Mo-Doped CuO Nanomaterial for Photocatalytic Degradation of Water Pollutants under Visible Light. *Catalysts* **2021**, *11*, 1198. [CrossRef]
39. Dasineh Khiavi, N.; Katal, R.; Kholghi Eshkalak, S.; Masudy-Panah, S.; Ramakrishna, S.; Jiangyong, H. Visible Light Driven Heterojunction Photocatalyst of CuO–Cu_2O Thin Films for Photocatalytic Degradation of Organic Pollutants. *Nanomaterials* **2019**, *9*, 1011. [CrossRef] [PubMed]
40. Durán, B.; Saldías, C.; Villarroel, R.; Hevia, S.A. In Situ Synthesis of CuO/Cu_2O Nanoparticle-Coating Nanoporous Alumina Membranes with Photocatalytic Activity under Visible Light Radiation. *Coatings* **2023**, *13*, 179. [CrossRef]
41. Mai, X.T.; Bui, D.N.; Pham, V.K.; Pham, T.H.T.; Nguyen, T.T.L.; Chau, H.D.; Tran, T.K.N. Effect of CuO Loading on the Photocatalytic Activity of $SrTiO_3$/MWCNTs Nanocomposites for Dye Degradation under Visible Light. *Inorganics* **2022**, *10*, 211. [CrossRef]
42. Hauchecorne, B.; Tytgat, T.; Verbruggen, S.W.; Hauchecorne, D.; Terrens, D.; Smits, M.; Vinken, K.; Lenaerts, S. Photocatalytic degradation of ethylene: An FTIR in situ study under atmospheric conditions. *Appl. Catal. B Environ.* **2011**, *105*, 111–116. [CrossRef]
43. Chen, L.; Xie, X.; Song, X.; Luo, S.; Ye, S.; Situ, W. Photocatalytic degradation of ethylene in cold storage using the nanocomposite photocatalyst MIL101(Fe)-TiO_2-rGO. *Chem. Eng. J.* **2021**, *424*, 130407. [CrossRef]
44. Montero, J.; Welearegay, T.; Thyr, J.; Stopfel, H.; Dedova, T.; Acik, I.O.; Österlund, L. Copper–zinc oxide heterojunction catalysts exhibiting enhanced photocatalytic activity prepared by a hybrid deposition method. *RSC Adv.* **2021**, *11*, 10224–10234. [CrossRef] [PubMed]
45. Luévano-Hipólito, E.; Torres-Martínez, L.M.; Fernández-Trujillo, A. Ternary ZnO/CuO/Zeolite composite obtained from volcanic ash for photocatalytic CO_2 reduction and H_2O decomposition. *J. Phys. Chem. Sol.* **2021**, *151*, 109917. [CrossRef]
46. Iazdani, F.; Nezamzadeh-Ejhieh, A. The photocatalytic rate of ZnO supported onto natural zeolite nanoparticles in the photodegradation of an aromatic amine. *Environ. Sci. Pollut. Res.* **2021**, *28*, 53314–53327. [CrossRef]
47. Condon, J.B.; James, B. *Surface Area and Porosity Determinations by Physisorption Measurements and Theory*, 1st ed.; Elsevier: Amsterdam, The Netherlands, 2006; pp. 55–90.
48. Sprynskyy, M.; Golembiewski, R.; Trykowski, G.; Buszewski, B. Heterogeneity and hierarchy of clinoptilolite porosity. *J. Phys. Chem. Sol.* **2010**, *71*, 1269–1277. [CrossRef]
49. Likhachev, D.; Malkova, N.; Poslavsky, L. Modified Tauc-Lorentz dispersion model leading to a more accurate representation of absorption features below the bandgap. *Thin Solid Films* **2015**, *589*, 844–851. [CrossRef]
50. Tauc, J. Optical properties and electronic structure of amorphous Ge and Si. *Mat. Res. Bull.* **1968**, *3*, 37–46. [CrossRef]
51. Pughazhenthiran, N.; Murugesan, S.; Valdés, H.; Selvaraj, M.; Sathishkumar, P.; Smirniotis, P.G.; Anandan, S.; Mangalaraja, R.V. Photocatalytic oxidation of ceftiofur sodium under UV-Visible irradiation using plasmonic porous Ag-TiO_2 nanospheres. *J. Ind. Eng. Chem.* **2022**, *105*, 384–392. [CrossRef]
52. Marakatti, V.S.; Halgeri, A.B.; Shanbhag, G. Metal ion-exchanged zeolites as solid acid catalysts for the green synthesis of nopol from Prins reaction. *Catal. Sci. Technol.* **2014**, *4*, 4065–4074. [CrossRef]
53. Barthel, H.; Rosch, L.; Weis, J. Fumed Silica-Production, Properties, and Applications. In *Organosilicon Chemistry II: From Molecules to Materials*; Auner, N., Weis, J., Eds.; Wiley: Hoboken, NJ, USA, 1996; Volume 1, pp. 761–778. [CrossRef]
54. Aboelfetoh, E.F.; Pietschnig, R. Preparation, characterization and catalytic activity of MgO/SiO_2 supported vanadium oxide based catalysts. *Catal. Lett.* **2014**, *144*, 97–103. [CrossRef]
55. Parida, S.K.; Dash, S.; Patel, S.; Mishra, B.K. Adsorption of organic molecules on silica surface. *Adv. Colloid Interface Sci.* **2006**, *121*, 77–110. [CrossRef]
56. Sabzehei, K.; Hadavi, S.H.; Bajestani, M.G.; Sheibani, S. Comparative evaluation of copper oxide nano-photocatalyst characteristics by formation of composite with TiO_2 and ZnO. *Solid State Sci.* **2020**, *107*, 106362. [CrossRef]
57. Sorbiun, M.; Shayegan Mehr, E.; Ramazani, A.; Fardood, S.T. Green Synthesis of Zinc Oxide and Copper Oxide Nanoparticles Using Aqueous Extract of Oak Fruit Hull (Jaft) and Comparing Their Photocatalytic Degradation of Basic Violet 3. *Int. J. Environ. Res.* **2018**, *12*, 29–37. [CrossRef]
58. Esmaili-Hafshejani, J.; Nezamzadeh-Ejhieh, A. Increased photocatalytic activity of Zn(II)/Cu(II) oxides and sulfides by coupling and supporting them onto clinoptilolite nanoparticles in the degradation of benzophenone aqueous solution. *J. Hazard. Mater.* **2016**, *316*, 194–203. [CrossRef]
59. Reza, K.M.; Kurny, A.; Gulshan, F. Parameters affecting the photocatalytic degradation of dyes using TiO_2: A review. *Appl. Water Sci.* **2017**, *7*, 1569–1578. [CrossRef]
60. De Lasa, H.; Serrano, B.; Salaices, M. Establishing Photocatalytic Kinetic Rate Equations: Basic Principles and Parameters. In *Photocatalytic Reaction Engineering*; Springer: Boston, MA, USA, 2005. [CrossRef]
61. Álvarez-Hernández, M.H.; Martínez-Hernández, G.B.; Avalos Belmontes, F.; Castillo-Campohermoso, M.A.; Contreras-Esquivel, J.C.; Artés-Hernández, F. Potassium Permanganate-Based Ethylene Scavengers for Fresh Horticultural Produce as an Active Packaging. *Food Eng. Rev.* **2019**, *11*, 159–183. [CrossRef]

62. Patdhanagul, N.; Srithanratana, T.; Rangsriwatananon, K.; Hengrasmee, S. Ethylene adsorption on cationic surfactant modified zeolite NaY. *Microporous Mesoporous Mater.* **2010**, *131*, 97–102. [CrossRef]
63. Bordiga, S.; Lamberti, C.; Bonino, F.; Travert, A.; Thibault-Starzyk, F. Probing zeolites by vibrational spectroscopies. *Chem. Soc. Rev.* **2015**, *44*, 7262–7341. [CrossRef]
64. Karimi Shamsabadi, M.; Behpour, M. Fabricated CuO–ZnO/nanozeolite X heterostructure with enhanced photocatalytic performance: Mechanism investigation and degradation pathway. *Mater. Sci. Eng. B Solid State Mater. Adv. Technol.* **2021**, *269*, 115170. [CrossRef]
65. Yu, Z.; Moussa, H.; Liu, M.; Schneider, R.; Wang, W.; Moliere, M.; Liao, H. Development of photocatalytically active heterostructured MnO/ZnO and CuO/ZnO films via solution precursor plasma spray process. *Surf. Coat. Technol.* **2019**, *371*, 107–116. [CrossRef]
66. Zhu, L.; Li, H.; Liu, Z.; Xia, P.; Xie, Y.; Xiong, D. Synthesis of the 0D/3D CuO/ZnO Heterojunction with Enhanced Photocatalytic Activity. *J. Phys. Chem. C* **2018**, *122*, 9531–9539. [CrossRef]
67. Bharathi, P.; Harish, S.; Archana, J.; Navaneethan, M.; Ponnusamy, S.; Muthamizhchelvan, C.; Shimomura, M.; Hayakawa, Y. Enhanced charge transfer and separation of hierarchical CuO/ZnO composites: The synergistic effect of photocatalysis for the mineralization of organic pollutant in water. *Appl. Surf. Sci.* **2019**, *484*, 884–891. [CrossRef]
68. Chabri, S.; Dhara, A.; Show, B.; Adak, D.; Sinha, A.; Mukherjee, N. Mesoporous CuO-ZnO p-n heterojunction based nanocomposites with high specific surface area for enhanced photocatalysis and electrochemical sensing. *Catal. Sci. Technol.* **2016**, *6*, 3238–3252. [CrossRef]
69. Ameta, R.; Solanki, M.S.; Benjamin, S.; Ameta, S.C. Photocatalysis. In *Advanced Oxidation Processes for Wastewater Treatment: Emerging Green Chemical Technology*; Ameta, S.C., Ameta, R., Eds.; Elsevier: Amsterdam, The Netherlands, 2018; Volume 1, pp. 135–175. [CrossRef]
70. Parrino, F.; Livraghi, S.; Giamello, E.; Ceccato, R.; Palmisano, L. Role of Hydroxyl, Superoxide, and Nitrate Radicals on the Fate of Bromide Ions in Photocatalytic TiO_2 Suspensions. *ACS Catal.* **2020**, *10*, 7922–7931. [CrossRef]
71. Azzolina Jury, F.; Polaert, I.; Estel, L.; Pierella, L.B. Synthesis and characterization of MEL and FAU zeolites doped with transition metals for their application to the fine chemistry under microwave irradiation. *Appl. Catal. A Gen.* **2013**, *453*, 92–101. [CrossRef]
72. Deng, C.; Zhang, J.; Dong, L.; Huang, M.; Li, B.; Jin, G.; Gao, J.; Zhang, F.; Fan, M.; Zhang, L.; et al. The effect of positioning cations on acidity and stability of the framework structure of Y zeolite. *Sci. Rep.* **2016**, *6*, 23382. [CrossRef]
73. Zholobenko, V.; Freitas, C.; Jendrlin, M.; Bazin, P.; Travert, A.; Thibault-Starzyk, F. Probing the acid sites of zeolites with pyridine: Quantitative AGIR measurements of the molar absorption coefficients. *J. Catal.* **2020**, *385*, 52–60. [CrossRef]